RESEARCH ARTICLE



Dynamical downscaling simulation of the East Asian summer monsoon in a regional Climate-Weather Research and Forecasting model

Qingquan Li^{1,2} | Tao Wang³ | Fang Wang^{1,2} | Xin-Zhong Liang⁴ | Chongbo Zhao¹ | Lili Dong¹ | Chunyu Zhao³ | Bing Xie¹

Correspondence

Tao Wang, Shenyang Regional Climate Center, Shenyang 110166, China. Email: nick_bsb@126.com

Funding information

National Natural Science Foundation of China, Grant/Award Number: 41790471; the National Key Scientific Research Plan of China, Grant/Award Number: 2016YFA0602200; the Second Tibetan Plateau Scientific Expedition and Research Program of China, Grant/Award Number: 2019QZKK0208; the Strategic Priority Research Program of the Chinese Academy of Sciences, Grant/Award Number: XDA20100304

Abstract

A regional Climate-Weather Research and Forecasting (CWRF) model with a 30-km horizontal resolution was applied to simulate the East Asian summer monsoon (EASM) and climate in China from 1980 to 2016. As compared with observations and reanalysis data, the model can reasonably reproduce the spatial distributions of the climatological mean atmospheric circulation and water vapour transport in East Asia, as well as the seasonal advance and retreat of EASM and rain bands. The correlation coefficient between the EASM circulation index in the simulation and reanalysis is .97. The model can well represent the geographic distributions of summer mean temperature and precipitation over most of China. However, model biases still exist, in particular the skill in the Yangtze-Huaihe River basin is relatively low. The simulated climatological mean temperature and precipitation deviations from observations may be related to the model's systematic circulation biases, with a thicker lower troposphere (i.e., higher temperature between 500 and 1,000 hPa) over most of China (except for the south and southwest) and a thinner one over the coastal oceans in summertime. Compared with the reanalysis, the model overestimates the land-ocean thermal contrast, which causes the South Asian High shifted to the north and east, as well as the subtropical high and tropical convective activity located further north and persisted longer. Consequently, more water vapour transports northward, leading to more precipitation over North China-Northeast China and less precipitation over the Yangtze and Huaihe River basin. Therefore, the enhanced land-ocean thermal contrast may be a major factor for the stronger EASM in the model, and corresponding precipitation and temperature biases in China. This analysis provides important information for further improving model performance in EASM simulation.

KEYWORDS

CWRF, dynamical downscaling, east Asian summer monsoon, land-ocean thermal contrast, regional climate model

¹Laboratory for Climate Studies, National Climate Center, China Meteorological Administration, Beijing, China

²Key Laboratory of Meteorological Disaster, Ministry of Education/Joint International Research Laboratory of Climate and Environment Change/ Collaborative Innovation Center on Forecast and Evaluation of Meteorological Disasters, Nanjing University of Information Science & Technology, Nanjing, China

³Shenyang Regional Climate Center, Shenyang, China

⁴Department of Atmospheric and Oceanic Science, University of Maryland, College Park, Maryland

1 | INTRODUCTION

Numerical climate models have been well recognized as essential tools and widely applied to address scientific issues concerning climate simulation and prediction. Global general circulation models (GCMs), commonly used in climate research, have remarkable biases in regional climate simulation due to their low resolution (Ding et al., 2006a, 2006b; Gao et al., 2012; Ou et al., 2013; Zhang et al., 2015, 2016; Xu et al., 2019; Liang et al., 2019; Li et al., 2020). In order to reduce the uncertainty of research results, regional climate models (RCMs) with higher resolution have been rapidly developed. RCMs are usually used in understanding physical processes, short-term climate prediction, climate change projection, and climate impact assessment (Giorgi, 2006; Xue et al., 2014; Giorgi and Gutowski, 2015; Tapiador et al., 2020). One of the most popularly used RCMs is Regional Climate Modelling system (RegCM), which is based on the Fifth-Generation Pennsylvania State University and University Corporation for Atmospheric Research Mesoscale Model (MM5) (Dickinson et al., 1989; Giorgi and Bates, 1989) and currently reached version 4.6 (Giorgi et al., 2011) through improving major physical parameterization schemes (Betts, 1986; Betts and Miller, 1986; Emanuel, 1991). On the other hand, the Weather Research and Forecasting (WRF) model, based on advanced supercomputing technology (Skamarock et al., 2005), adopts a modular design with mutual program modules, which is convenient for users to carry out further development and research. On this basis, the CWRF (Climate-Weather Research and Forecasting) model was established and has been employed in climate simulation research (Liang et al., 2005a, 2005b, 2005c, 2006b, 2012).

To study the summer rainfall over China, Liu et al. (2008) reproduced the extreme rainfall in the Yangtze River basin in summer 1998 with CWRF and found that the east-west boundary and the main controlling factor of the circulation had an important impact on climate simulation. Zeng et al. (2008) analysed the outputs of 120-hour ensemble predictions with eight parameterized combination schemes, including radiation processes, cloud physics and the boundary layer. The results showed that CWRF has high forecasting capability for regional rainfall over China, in which the cumulus parameterization scheme is the most important factor in short-term forecasts. Moreover, Zeng et al. (2009) used the CWRF model to successfully simulate the vertical distribution of persistent precipitation and temperature in southern China in winter 2008, and revealed that the terrain can not only affect the formation and maintenance of freezing rain over the Hengduan and Nanling Mountains, as

well as their adjacent mountainous areas, by changing the frontal area, but also change the circulation fields to affect the large-scale rainfall intensity and heavy rainfall areas.

Liu *et al.* (2008) compared the simulations of regional precipitation over China between the early version of CWRF and RegCM3, and found CWRF to be significantly better than RegCM3, in which the geographic distribution of precipitation in China and the precipitation area of the pre-flood season in South China simulated by CWRF were consistent with observations in May 1998, while the simulation of RegCM3 had significant errors. Besides the illusive rainfall over the south and east of the Qinghai–Tibet Plateau, two centre's of heavy rainfall over the region south of the Yangtze River in June 1998 were successfully captured by CWRF, but only one centre was captured by RegCM, with large bias in locations.

Liang *et al.* (2018) demonstrated that CWRF performs better overall than RegCM4.6, as measured by various quantitative metrics. For all seasons, CWRF shows higher skill than RegCM4.6 in simulating interannual variations of precipitation, temperature, and humidity. In particular, CWRF captures the two major summer monsoon rain bands along the Yangtze River and across South China more realistically than RegCM4.6. Furthermore, CWRF exhibits outstanding performance in reproducing the 95th percentile of daily precipitation and the diurnal temperature range.

The application of CWRF in the East Asian domain just started, and to date has focused mainly on the general characteristics of temperature and precipitation seasonal-interannual variations, lacking systematic evaluation of the model ability to simulate the most critical regional climate feature: the East Asian monsoon system. In particular, it is vital to understand how well the model simulates the EASM processes associated with the seasonal advance and interannual variation of precipitation and temperature, the relationships between atmosphere circulation and moisture transport and between the Western Pacific Subtropical High and precipitation, as well as the underlying physical mechanisms that may cause the model biases in these aspects.

In this paper, CWRF is used to simulate summer temperature, precipitation and atmospheric circulation, as well as their couplings with water vapour, in East Asia during 1980–2016. The simulation performance in the East Asian monsoon region is comprehensively analysed, and the model bias and its possible causes are revealed, which is conducive to further improvement in CWRF's application in East Asia.

The rest of the paper is organized as follows. Section 2 describes the model, experiment, and methods. Section 3 analyses the model performances in simulating rainfall,

surface air temperature, and major members of the East Asian summer monsoon systems, including the Western Pacific Subtropical High (WPSH), South Asian High (SAH), and wind fields, as well as water vapour and thermal conditions. Section 4 summarizes the major conclusions.

2 | MODEL, EXPERIMENT AND METHODS

2.1 | Description of model and numerical experiments

CWRF, as an extension of WRF in climate research, has been mainly improved in four aspects (Liang et al., 2005a, 2005b, 2005c, 2006b, 2012; Choi et al., 2007, 2013; Choi and Liang, 2010; Ling et al., 2011, 2015; Yuan and Liang, 20112015; Liang and Zhang, 2013; Zhang et al., 2013; Xu et al., 2014; Qiao and Liang, 2015, 2016a,b): (a) Consistent treatments for surface and lateral boundary conditions to improve surface-atmosphere interactions and optimize energy and mass fluxes from GCM to RCM; (b) Enhancing physical parameterization schemes, such as the land, terrestrial hydrology, lake, ocean, and planetary boundary layer processes, to improve surfaceatmosphere interactions; (c) Full coupling among new parameterization schemes, including cloud microphysical processes, convective clouds, cloud formation, and radiative transport, to improve convective-cloud-radiation interactions; (d) Using the same physical constants, tunable parameters, solar height, and saturated water vapour equations to ensure system consistency among all the modules. Finally, a large amount of sensitivity tests and rigorous verification processes have been undertaken with CWRF.

configuration and main parameterization schemes of CWRF used in this study follow Liang et al. (2018) and are shown in Table 1. The CWRF computational domain covers approximately (8°-59°N,58°-162°E) based on the Lambert conformal map projection centred at (35.18°N, 110°E) with a total of 232×172 grid points at 30-km spacing. By default, CWRF uses 36 terrain-following vertical levels with the top boundary at 50 hPa (Liang et al., 2012). Liu et al. (2008) demonstrated that this domain is optimal for modelling China's regional climate, which is determined by interactions between the planetary circulation (as forced by lateral boundary conditions) and East Asian surface processes, including orography, soil, vegetation and coastal oceans. In the buffer zones, located across 14 grids along the four edges of the domain, varying lateral boundary conditions were specified using a dynamic relaxation technique with

TABLE 1 Configuration and main parameterization schemes of CWRF

	Dynamic core	Non-hydrostatic WRF
Dynamics configuration	Vertical levels	36
Lateral boundary conditions	Buffer zones	14 grids
	Dynamic relaxation	Linear-exponential nudging coefficients (Liang et al., 2001)
Surface boundary conditions	Land	USGS 24 dominant categories (Liang <i>et al.</i> , 2005a; Xu <i>et al.</i> , 2014)
Physics configuration	Cumulus	ECP penetrative convection (Qiao and Liang, 2017) UW shallow convection (Bretherton and Park, 2009)
	Microphysics	GSFCGCE (Tao et al., 2003)
	Cloud	XRL (Xu and Randall, 1996; Liang <i>et al.</i> ,)
	Aerosol	MISR (Kahn <i>et al.</i> , 2005, 2007; Zhao <i>et al.</i> , 2009)
	Radiation	GSFCLXZ (Chou and Suarez, 1999; Chou et al., 2001)
	PBL	CAM (improved Holtslag and Boville, 1993) ORO (Rontu, 2006; Liang et al., 2006b)
Surface	Land	CoLM-CSSP conjunctive surface–subsurface physical and hydrological processes (Choi, 2007, 2013; Liang et al., 2005a, 2005b)
	Ocean	UOM upper ocean with transient air–sea interactions (Ling et al., 2011, 2015)

linear-exponential nudging coefficients that decrease toward the surface and the inner boundaries (Liang $et\ al.$, 2001). Both the horizontal and vertical resolutions for CWRF are relatively finer than most RCMs applied for long-term simulations in the region, which typically use \sim 50-km grids and \sim 20 levels (Liang $et\ al.$, 2018).

In this study, the CWRF model was driven by the European Centre for Medium-Range Weather Forecasts interim reanalysis (ERA-Interim; Dee *et al.*, 2011), which is considered as one of the best available proxies for observations, including many physical variables, such as surface pressure, temperature, geopotential height,

moisture, wind, etc. The horizontal resolution of ERA-Interim data is 0.75° longitude by 0.75° latitude. The data of four times per day were used. The simulations were initiated on October 1, 1979 and integrated continuously through to December 31, 2016. The initial 3 months were considered as a spin-up, and the results from January 1, 1980 to December 31, 2016 were used in the subsequent analysis.

2.2 | Data and methods

In addition to the CWRF simulation results mentioned above, as the reference for model evaluation, observational data composed of a gridded (0.25°longitude by 0.25° latitude) daily analysis of precipitation and surface air (2 m) temperature, based on in situ measurements at 2416 stations in China from 1961 onward (Wu and Gao, 2013), were employed. Moreover, the ERA-Interim data with horizontal resolution of 0.25° longitude by 0.25° latitude and 17 vertical levels were adopted to validate the simulation results. Many physical variables were used, such as geopotential height, wind, relative humidity, and temperature, etc. For the convenience of comparing simulations with observations, the simulated precipitation and air temperature at 2 m were interpolated onto the grids of observational data, and the simulation results of other circulation variables were interpolated onto the grids of ERA-Interim data by using a bilinear method.

The model simulations were assessed using the temporal correlation coefficient (TCC) from the World Meteorological Organization (WMO, 2006). The effects of different latitudes are taken into account when calculating the regional average. In order to assess the performance of CWRF in simulating the seasonal and interannual variations of EASM, it is necessary to define a circulation index that characterizes the intensity of the summer monsoon. This study adopted Zhang *et al.* (2003) to define the EASM index as the differences in 850-hPa zonal mean wind anomalies between the monsoon trough (10°–20°N, 100°–150°E) and the subtropical region (25°–35°N, 100°–150°E) over East Asia in summer. Below, summer refers to June, July and August, and climatological average is calculated from 1980 to 2016.

3 | RESULTS

3.1 | Surface air temperature and rainfall over China

Figure 1 shows that the CWRF simulation is close to the observed mean surface air temperature spatial

distribution over China in summer (June–July–August). The intensity and location of high-temperature centres are reproduced well by CWRF. Except for the northwestern China, the model temperature biases are small between the southern and northern parts of China. The mean temperatures in most areas of China in summer are above 16°C (Figures 1a,b). The simulated temperature biases mostly range between -2° C and 2° C, except with notable warm biases located in the Tarim basin of Xinjiang and cold biases in the vicinity of the Hengduan and Himalayan Mountains (Figure 1c). The TCCs of summer temperatures are high in most regions of China, with skills exceeding 0.6 over Northeast and Northwest China, but they are relatively low in the Yangtze–Yellow River basin.

As influenced by the East Asian monsoon, air temperature in East China is characterized by simultaneous rainfall and heat (Li et al., 2005). The time-latitude crosssection of surface air temperature averaged over East Asia (Figure 2) shows that, from March, air temperatures rise mainly in the middle and high latitudes over the area north of 35°N. At the end of March, temperatures in the middle and high latitudes approach 0°C, while those in the low latitudes rise slowly. From April onwards, temperatures rise rapidly from south to north. In July, temperatures reach the maximum in a year, and the 20°C isotherm approaches 50°N. In mid-August, temperatures begin to decrease rapidly. CWRF realistically reproduces the observed temperature seasonal variation. However, the simulated temperatures are higher than observations, with the model warm centre located more northward and lasting longer in summer. The northernmost isotherm of 28°C approaches 35°N from the beginning of July to the end of August. Besides, the isotherm of 20°C exceeds 50°N and its duration is consistent with that of the 28°C isotherm (Figure 2b).

Precipitation is one of the most important variables of societal relevance, such as drought and floods (Hu et al., 2019). Figure 3 shows the distributions of summer mean precipitation and deviation in China. Observations show that the summer rainy area in China is located in the East Asian monsoon area, including South China, North China and Northeast China. CWRF underestimates the overall rainfall amount, with negative biases over South China and positive biases over North China (Figures 3a,b). Notably, the model captures the observed rainfall well over large-scale terrain, such as the Sichuan basin, Nanling Mountains, Dabie Mountains, Mountains, Changbai Yanshan and Mountains (Figure 3b). The absolute biases of precipitation in most areas of North China and Tibet is less than 1 mm/day, while the positive biases are 1-2 mm/day in some areas of Northeast China, North China, and the provinces of

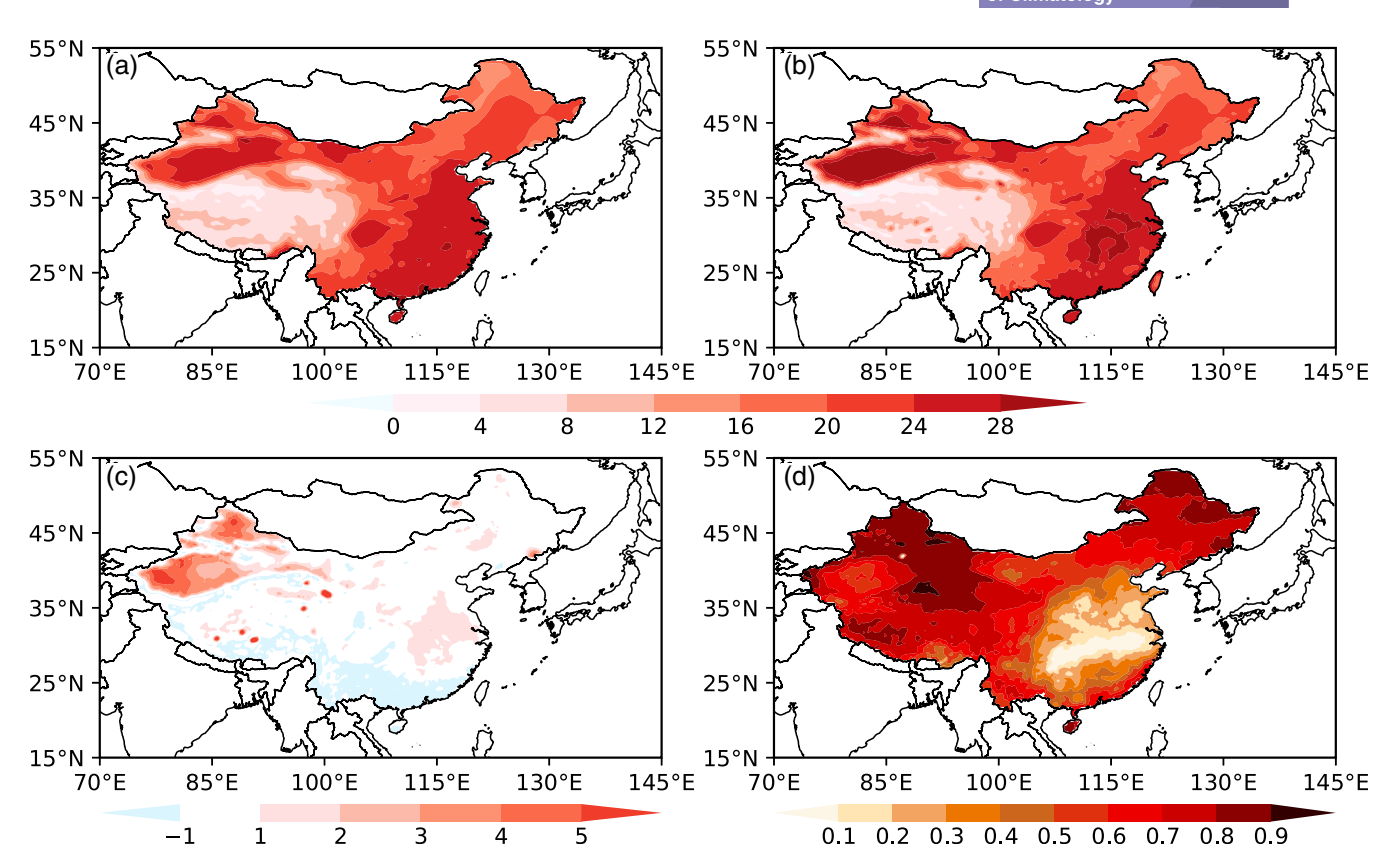


FIGURE 1 Climatologically averaged surface air temperature over China in summer (June–July–August; units: °C): (a) observation; (b) simulation; (c) simulation minus observation; (d) TCC (>0.3 denotes statistical significance at the 95% confidence level) [Colour figure can be viewed at wileyonlinelibrary.com]

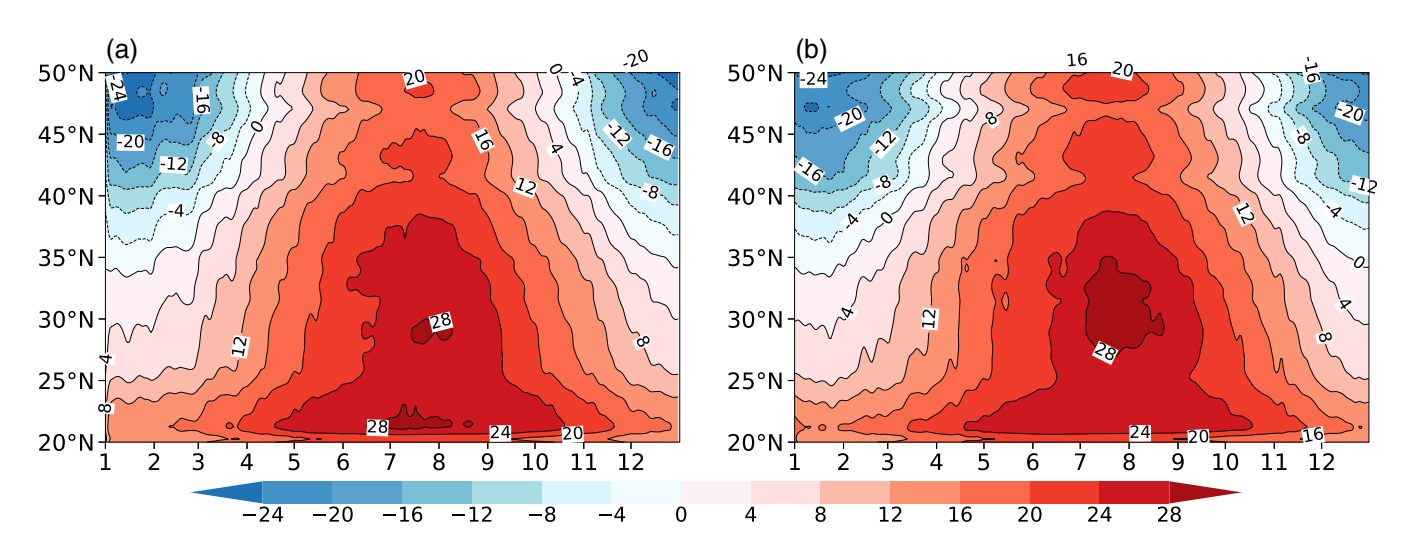


FIGURE 2 Latitude–time cross-sections of averaged surface air temperature along 110°–120°E from January to December (units: °C): (a) observation; (b) simulation [Colour figure can be viewed at wileyonlinelibrary.com]

Gansu and Qinghai. The negative biases in South China are generally around 1–2 mm/day, except in Zhejiang, Fujian and Yunnan provinces exceeding 2 mm/day (Figure 3c). Figure 3 shows that the simulation skills are generally high in Northeast China, Southeast (coastal) China, Tibet, and parts of Xinjiang, where TCCs are all

above 0.3 and statistically significant at the 95% confidence level. The skills are lower over other regions. Besides, high skills are mostly located in the areas with large-scale terrains, which may be related to the CWRF's better performance in simulating the topography-forced rainfall distribution. Because CWRF is designed with

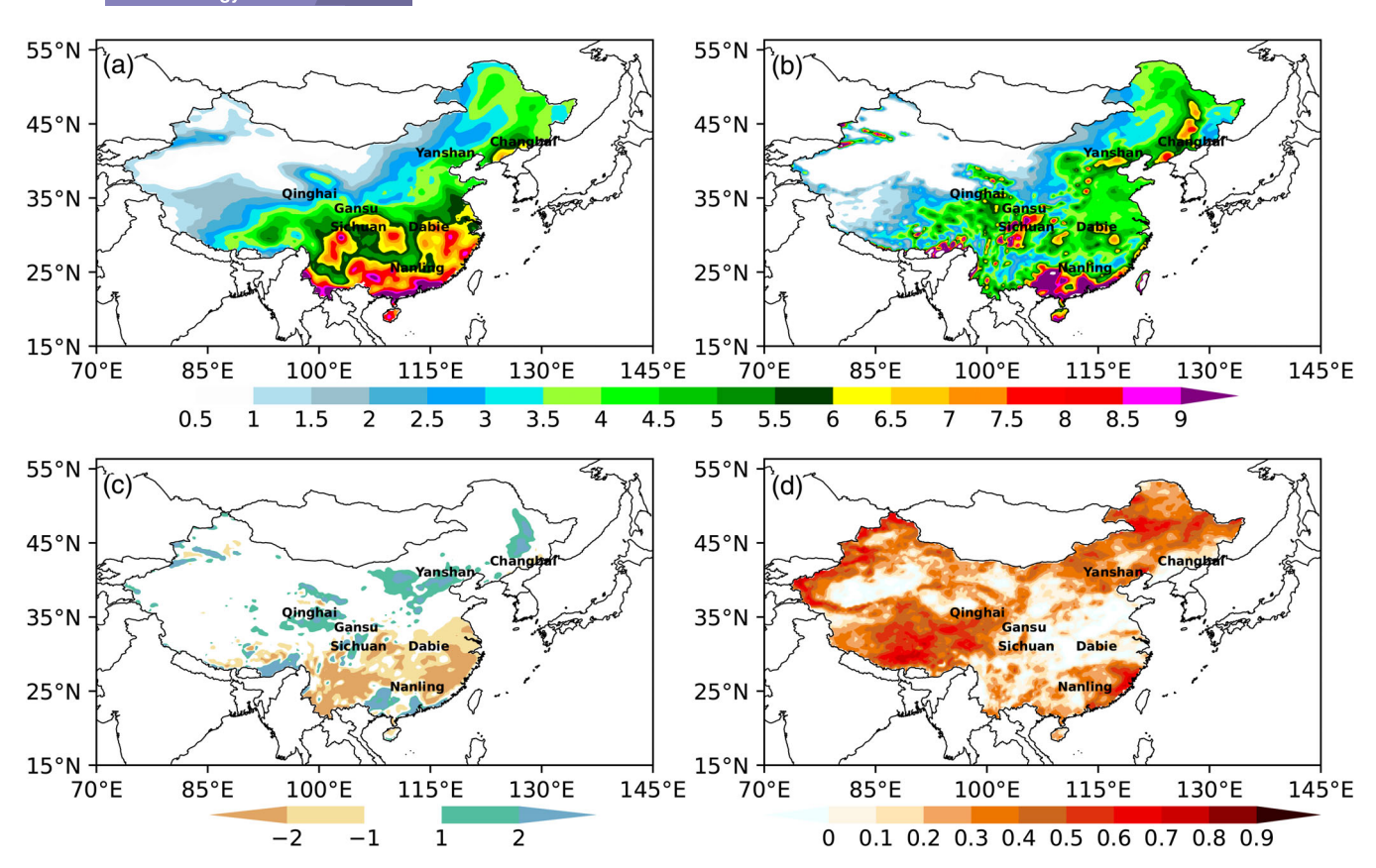


FIGURE 3 Climatologically averaged precipitation over China in summer (June–July–august; units: Mm/day): (a) observation; (b) simulation; (c) simulation minus observation; (d) TCC (>0.3 denotes statistical significance at the 95% confidence level) [Colour figure can be viewed at wileyonlinelibrary.com]

advanced physical parameterizations to better represent surface-atmosphere interaction processes (see Section 2.1), it can well simulate the topography related rainfall distribution (Liang *et al.*, 2012, 2018).

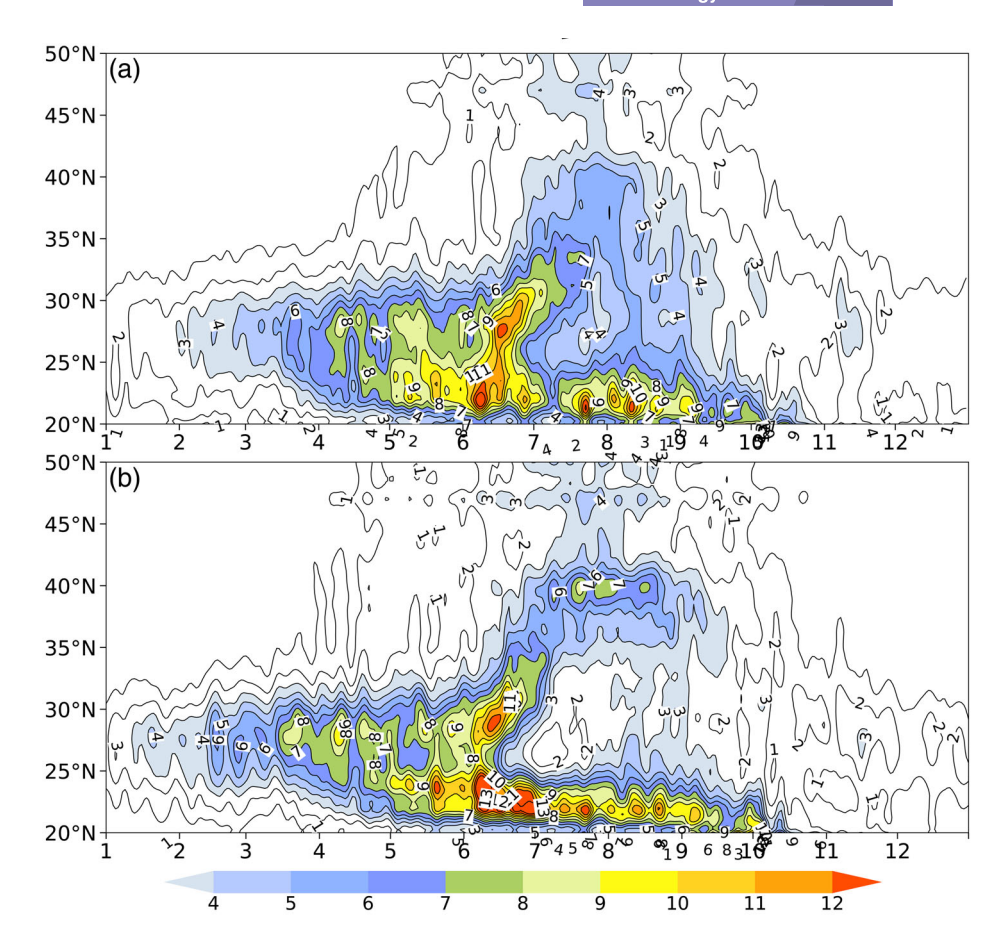
As compared in Figures 1 and 2, CWRF overestimates temperatures over the Yangtze-Huaihe River basin, and hence the land-ocean thermal contrast that leads to a stronger EASM. As a result, the model underestimates rainfall over the basin but overestimates it over the north (Figure 3c). Figure 3d further shows that TCC values are relatively low in the basin and higher in the north. This indicates that the model simulates rainfall interannual variations in the basin overall worse than in the north. Note that precipitation interannual variability is larger in the basin than in the north, and that precipitation can be more easily modelled under stable than convective conditions. This may be one of the reasons why relatively low skills appear over the basin, where convective precipitation prevails with large variability in summer, while the skill is much better over the north, where stable precipitation is more frequent.

Figure 4 shows that the rain band in East China clearly possesses seasonal characteristics of a northward advance and southward retreat under the influence of the East Asian monsoon. The rain band is located around 27°N over South China before May, with a maximum rainfall amount of 8 mm/day. The locations of simulated precipitation are roughly consistent with observations, but the starting time is about five pentads earlier due to a general, slight overestimation of rainfall amount. The first northward jump of the rain band results in a rapid increase of rainfall in early May. In June, the rainfall amount reaches a maximum (exceeding 12 mm/day), with two rainfall centres respectively appearing in the north and south. The south centre is located around 23°N, which is called the pre-flood season in South China, and the north centre is located around 27°N, which is called the Meiyu season in the Yangtze River basin.

The rain band continues to advance northward in early July, reaching the north most location at 42°N in early August, with the rainfall mainly occurring in North China and Northeast China. Less rainfall appears around 30°N and lasts for nearly 20 days, which is related to the long-term maintenance of the subtropical high over this region and is called the summer drought over the Yangtze River basin. The simulation results are similar to observations, but the rainfall amount is overestimated by

■ RMetS

FIGURE 4 Latitude-time crosssections of averaged daily precipitation along 110°-120°E from January to December (units: mm/day): (a) observation; (b) simulation [Colour figure can be viewed at wileyonlinelibrary.com



2 mm/day in North China. Compared with observations, the simulated rain band shifts northwards by 2-3° and lasts about 1 month longer till September 10. The dry summer period is obviously longer than that observed, lasting from early July to early August with rainfall underestimated by 1-2 mm/day. This may be because the model simulates a stronger summer monsoon, causing larger rainfall over North China and lower amount over the Yangtze-Huaihe River basin. The observed main rain band gradually retreats from North China to South China starting in mid-August, but the simulation occurs nearly a month later and more abruptly (Figure 4b).

3.2 Atmospheric circulation and its connections with temperature and rainfall

3.2.1 Potential height and thickness

Compared with the observed 500-hPa geopotential height in summer, CWRF can capture well the characteristics of the large-scale circulation pattern (Figures 5a,b). High TCC skills can be seen over most of East Asia (Figure 5d). There are westerly flows in the middle and high latitudes and subtropical high over the east of the

East China Sea. The simulated subtropical high ridge is consistent in latitude with the reanalysis. The simulated ridge line locates around 25°N, although WPSH shifts slightly eastward (Figure 5b). The model departures from the reanalysis (Figure 5c) are positive in Mongolia and East China, with a maximum of 20 gpm near the Changbai Mountains. This positive height bias is conducive for the model to simulate warmer temperature and smaller precipitation in the eastern region (Figures 1 and 3).

The WPSH is a key component of the East Asian monsoon system and closely associated with the rainfall distribution over China (Si et al., 2019). Figure 6 shows the time-latitude cross-section of 500-hPa mean height along 126°E, with the 5,840-gpm contour denoting the location of the main body of WPSH. The model captures well WPSH's seasonal variation. In winter, WPSH stably locates over the South China Sea and the ocean to the east of the Philippines. In the second pentad of March, WPSH begins to shift gradually northwards, which corresponds to the pre-flood period of South China. It jumps northwards for the first time in the first pentad of May, then stays north of South China for a short period. It shifts rapidly northwards, crosses over 27°N, and arrives over the Yangtze River basin in middle June, which is its

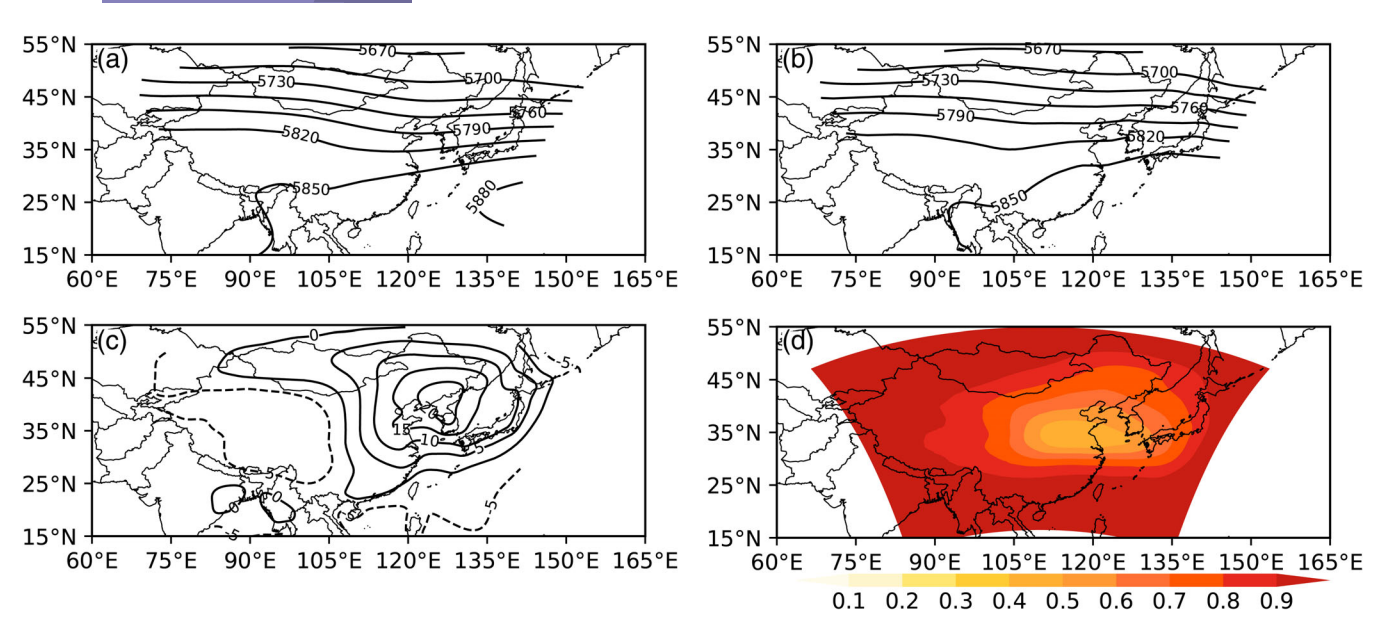


FIGURE 5 Climatologically averaged geopotential height at 500 hPa over East Asia in summer (June–July–August; units: Gpm): (a) observation; (b) simulation; (c) simulation minus observation; (d) TCC (>0.3 denotes statistical significance at the 95% confidence level) [Colour figure can be viewed at wileyonlinelibrary.com]

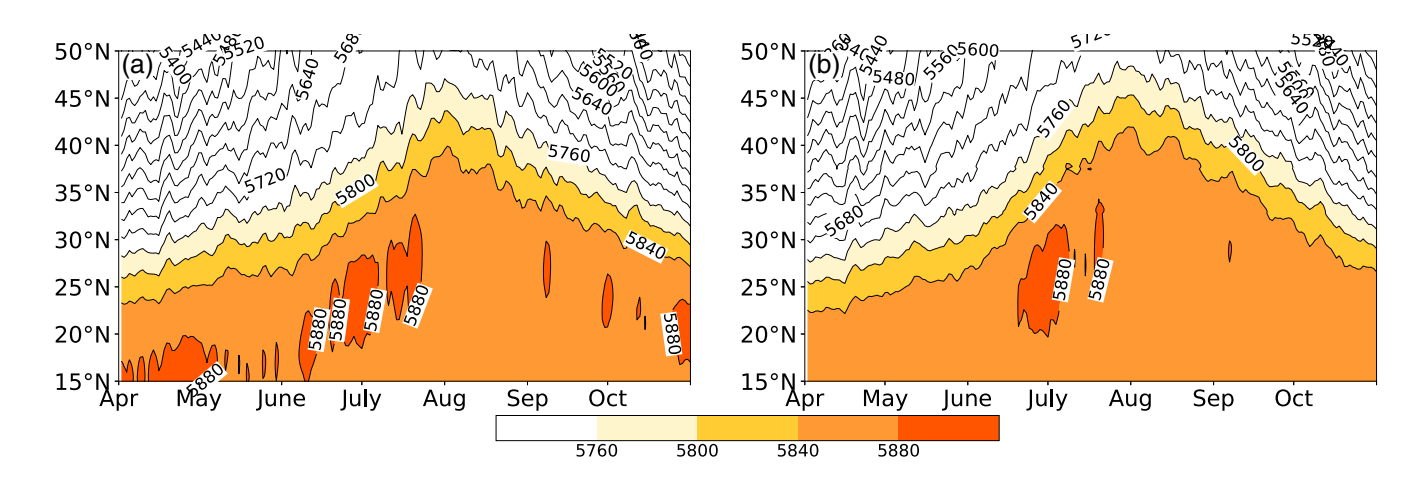


FIGURE 6 Latitude–time cross-section of averaged geopotential height at 500 hPa along 126°E from January to December (units: gpm): (a) reanalysis; (b) simulation [Colour figure can be viewed at wileyonlinelibrary.com]

second jump and corresponds to the so-called Meiyu period. From middle-late July, WPSH jumps rapidly northwards for the third time and reaches the Yellow River basin and North China before then arriving at its northernmost position (42°N) in the first pentad of August.

Thereafter, WPSH retreats rapidly southwards in the third pentad of August. It stays over the Yangtze and Huaihe river basins for a short period in the first to third pentads of September, and then retreats continuously southwards. Compared with the reanalysis, CWRF simulates WPSH well in its seasonal variation, although the dates of the first and second jumps are slightly delayed

and the location shifted southwards by 1° (Figure 6b). The model shifts WPSH northwards by 3°-5° in the third jump and its northernmost margin by 2°, with its duration lasting longer until the sixth pentad of August. As a result, the rain band stays over North China and Northeast China during this period and the rainfall amounts are larger than observed. The long-term maintenance after the third jump leads to a delayed retreat. The northernmost margin is shifted northwards by 3°, reaching 37°N. Overall, the seasonal variations of WPSH are simulated well by CWRF, except for lying more northwards, thus leading to the overestimated rainfall and temperature in North China.

Figure 7 shows the model biases of the thickness between 500 and 1,000 hPa in the middle and low troposphere. Given the heat source over land, the maximum thickness exceeds 5,200 gpm, located over the Qinghai-Tibet Plateau in summer. In contrast, the minimum thickness (less than 4,720 gpm) occurs over the oceans. CWRF simulates these characteristics in a close agreement with the reanalysis. On the other hand, the model shows positive thickness biases mainly located over the northeast of East Asia, centred over the Changbai Mountains, and negative bias over the ocean (Figure 7c). Thus, the model produces a stronger thermal response of the atmosphere overland than the ocean, and so overestimates the land-ocean temperature difference. As a result, the model simulates a stronger EASM system, causing the rain band shifted northwards along with more rainfall over North China and less rainfall over South China (Figures 3 and 1).

3.2.2 Wind fields

The model simulates the summer mean wind circulation well at 850 hPa (Figure 8). The cross-equatorial airflows converge around (120-125°E, 25°N), and then form strong monsoonal flows northwards along the western edge of WPSH. The strong airflows across North China come from the south of the Yangtze River and the East China Sea (Figure 8). Compared with the reanalysis, the simulated southwesterly winds are stronger, especially in the area north of 30°N. The model produces anticyclonic circulation biases over the Sea of Japan (Figure 8c), which may contribute to stronger southwesterly winds over North China and Northeast China, thus leading to more rainfall over North China. Correspondingly, there anticyclonic circulation biases at 200 hPa (Figure 9c) along with positive biases in mean thickness between 500 and 1,000 hPa (Figure 7c) as well as in mean geopotential height at 500 hPa (Figure 5c). Other weaker anticyclonic circulation biases occur over the Bay of Bengal (Figure 8c). The easterly winds of the front weaken the southwest monsoon, leading to less rain over South China (Figure 3c).

The simulated summer mean winds at 200 hPa are consistent with those of the reanalysis (Figures 9a,b). The main body of the South Asian high is located over the Qinghai-Tibet Plateau, and the boundary between the easterly and westerly flows is shifted northwards to around 27°N. The westerly jets are consistently located at around 40°N, but the simulated maximum speed of 24 m/s is less than that of the reanalysis. The easterly flows are similarly located over the south of East Asia. The model produces prominent anticyclonic wind biases over North China (Figure 9c), thus leading to stronger (weaker) westerly winds in the north (south) of the westerly jet. Associated with these, a meridional dipole may cause the South Asian high to shift from the Qinghai-Tibet Plateau to North China, contributing to the northward location of WPSH and thus leading to a northward rain band (Liang and Wang, 1998).

Figure 10 shows a latitude-height section of zonal wind speed. CWRF simulates the distribution well as in the analysis. The boundary between the easterly and westerly flows consistently locates around 27°N in the

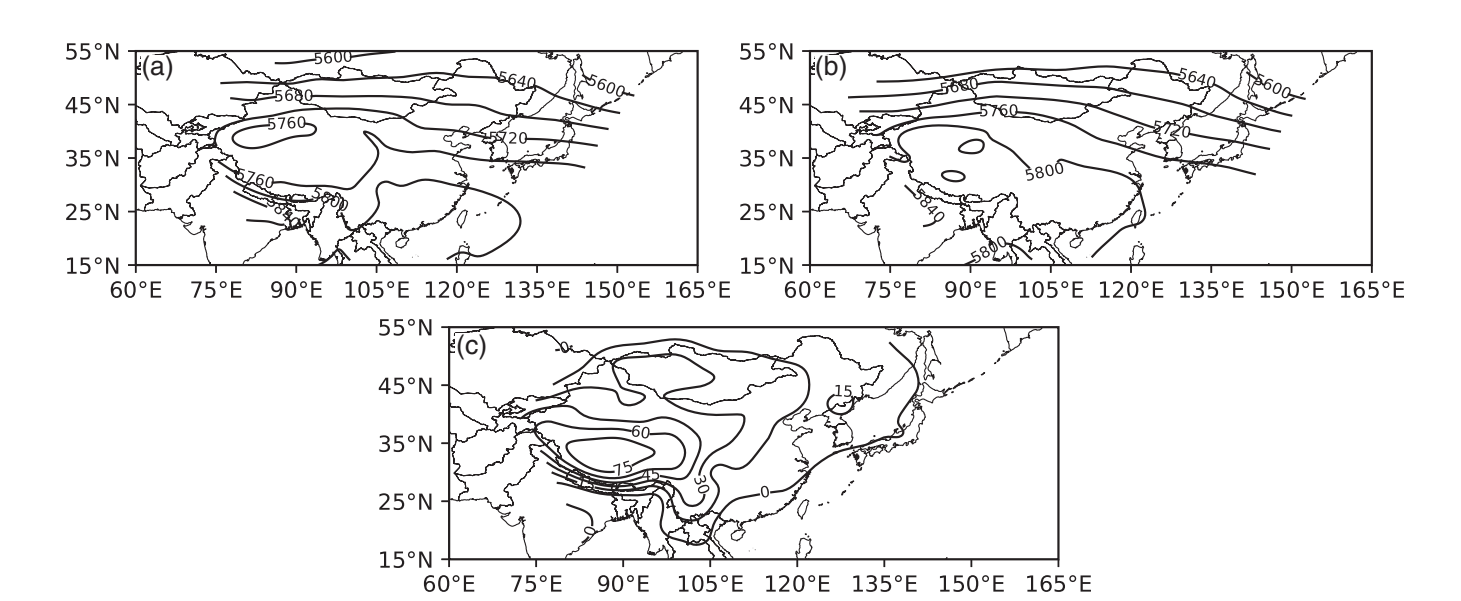


FIGURE 7 Climatologically averaged 500-1,000 hPa thickness in summer over East Asia in summer (June-July-August; units: gpm): (a) observation; (b) simulation; (c) simulation minus observation

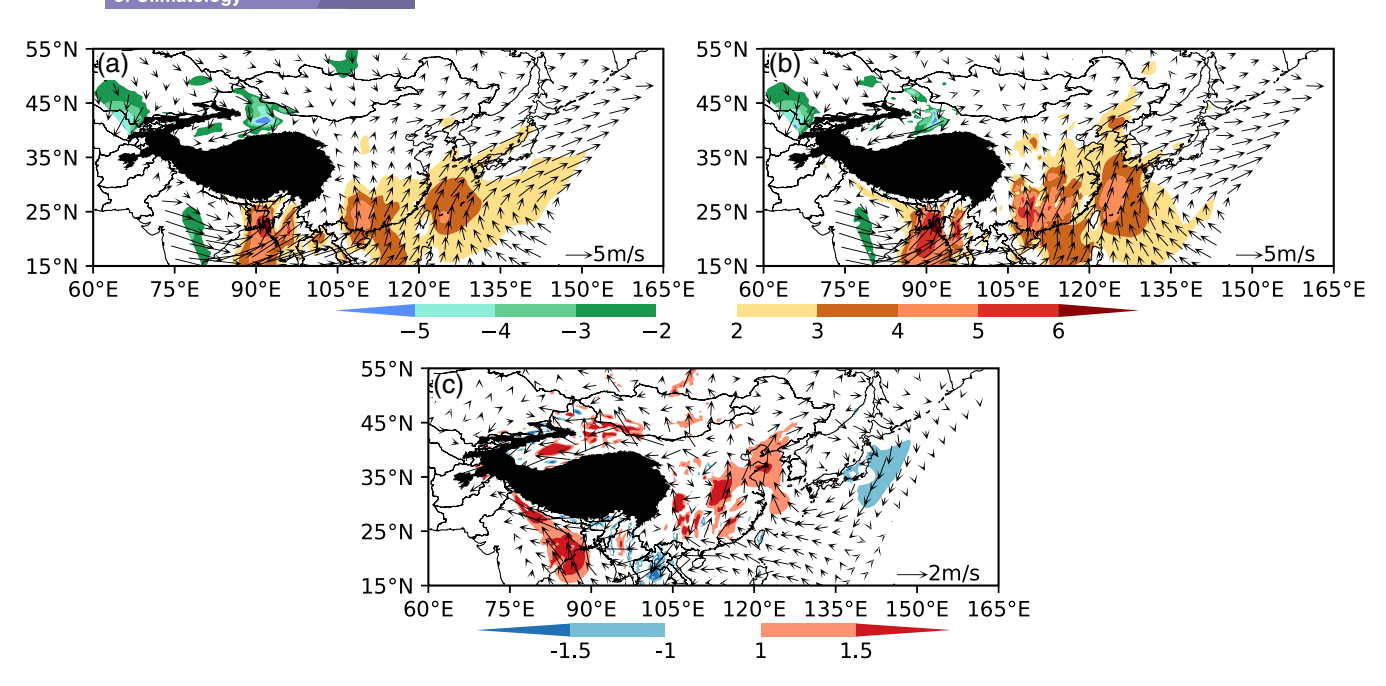


FIGURE 8 Climatologically averaged wind at 850 hPa in summer (June–July–August; units: m/s; arrows and colour shading represent wind vectors and meridional winds, respectively): (a) observation; (b) simulation; (c) simulation minus observation [Colour figure can be viewed at wileyonlinelibrary.com]

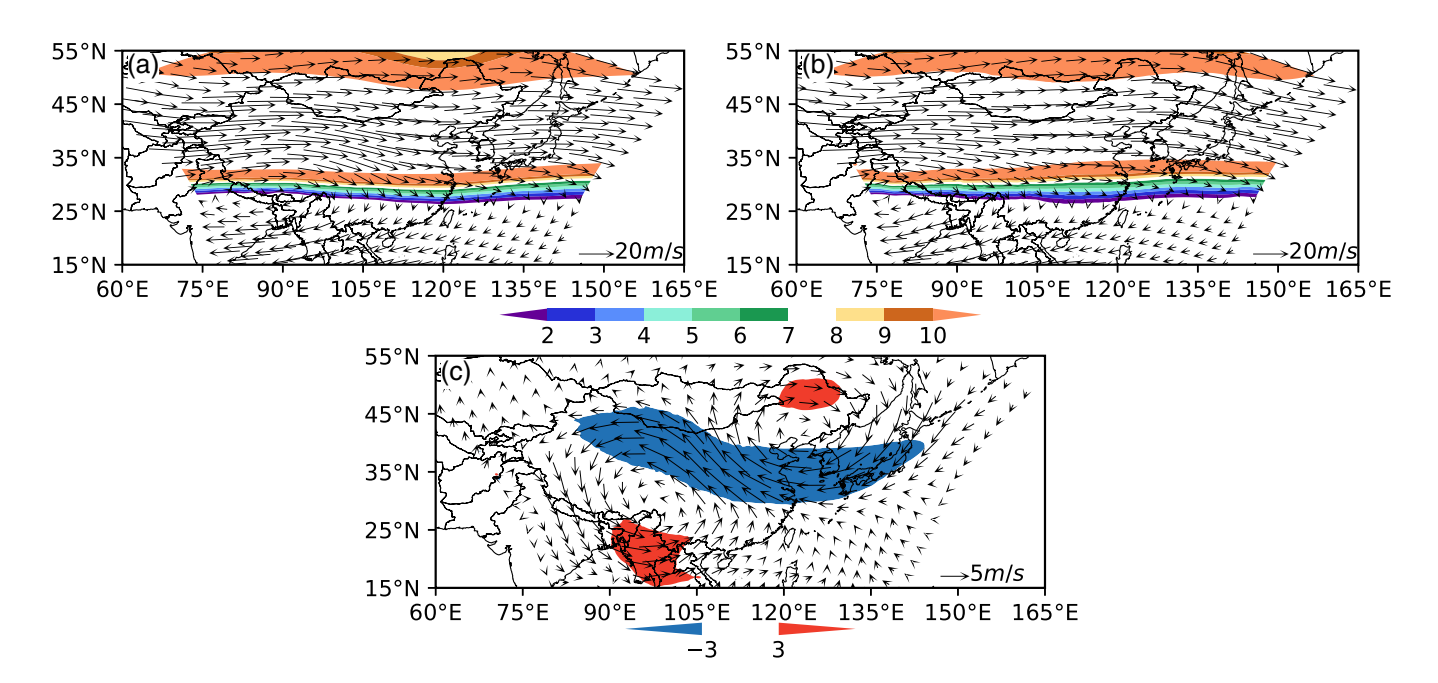


FIGURE 9 Climatologically averaged wind at 200 hPa in summer (June–July–august; units: m/s; arrows and colour shading represent wind vectors and zonal winds, respectively): (a) observation; (b) simulation; (c) simulation minus observation [Colour figure can be viewed at wileyonlinelibrary.com]

upper troposphere. Located to the north is the westerly jet, with the centre at around 40°N at 200 hPa, although the model underestimates its maximum speed by 5 m/s. Located to the south is the easterly jet, with a maximum speed of over 15 m/s, which contributes to the maintenance of the South Asian high. The easterly and westerly

flows of the boundary layer occur in the south and north flanks of WPSH, respectively (Figures 10a,b). The model biases are small (Figure 10c). The maximum bias of -4 m/s mainly occurs at $25^{\circ}-40^{\circ}N$ in the upper troposphere, leading to a weak westerly jet. A positive bias occurs in the areas south of $25^{\circ}N$ and north of $45^{\circ}N$.

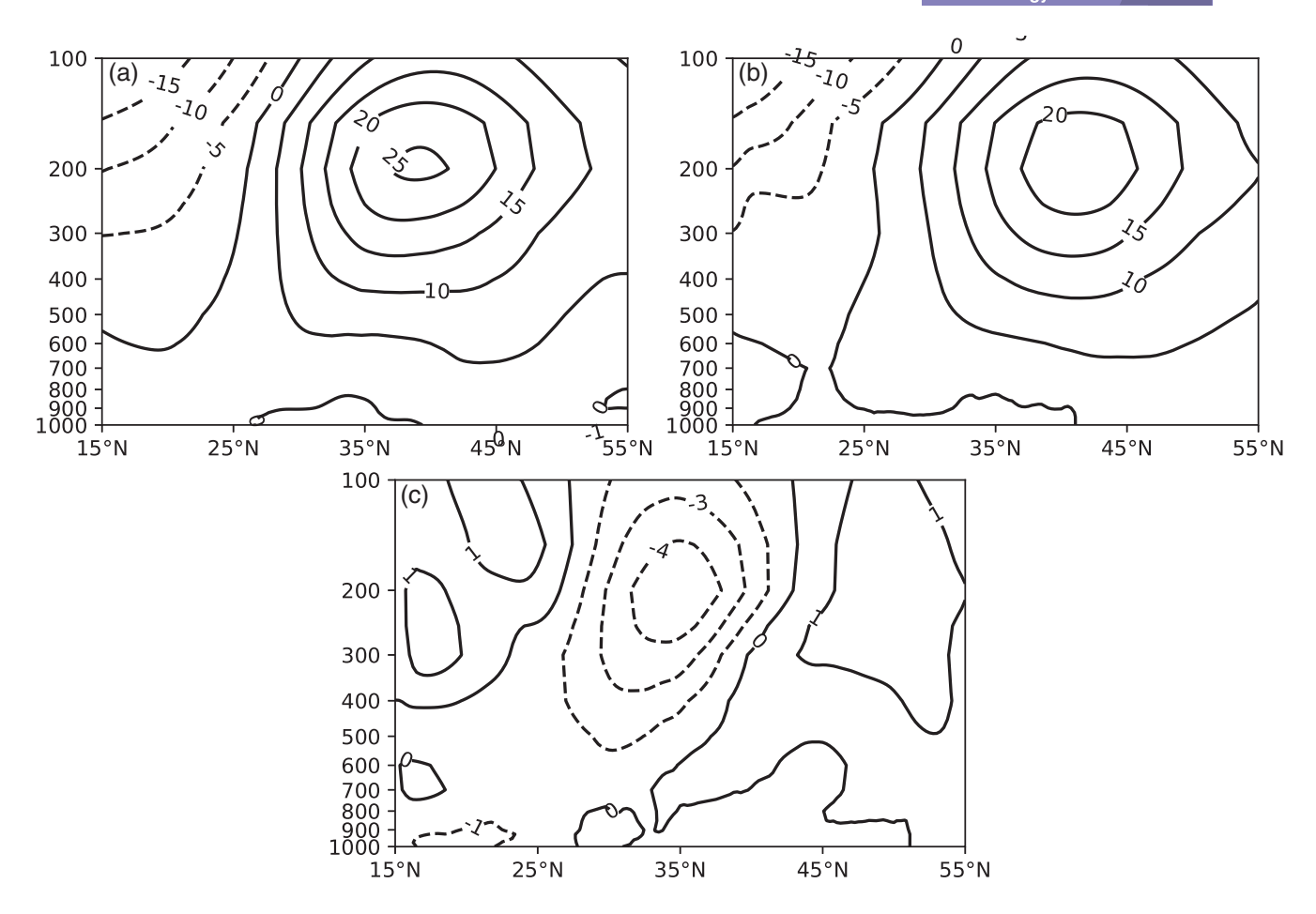


FIGURE 10 Height-latitude cross-sections of averaged zonal wind along 110°-120°E in summer (June–July–August; units: m/s): (a) observation; (b) simulation; (c) simulation minus observation

Furthermore, the interannual correlation coefficient during 1980–2016 between the EASM indexes simulated by CWRF and in the reanalysis is .97. This reflects that the simulated interannual variability of the monsoon circulation system is highly consistent with the reanalysis (Figure 11). The long-term average value of the EASM index is 0.03 in the model versus –0.02. This implies that CWRF simulates a stronger EASM system than the reanalysis.

3.2.3 | Water vapour transport and pseudo-equivalent potential temperature

The distribution of the vertically integrated vapour flux simulated by CWRF is consistent with that of the reanalysis. There are mainly three moisture channels in the East Asian summer monsoon (Figures 12a,b). One channel is the cross-equatorial moisture from the subtropical Mascarene high over the South Indian Ocean, in which the moisture flows across the Bay of Bengal and the Indochina Peninsula, and reaches the South China

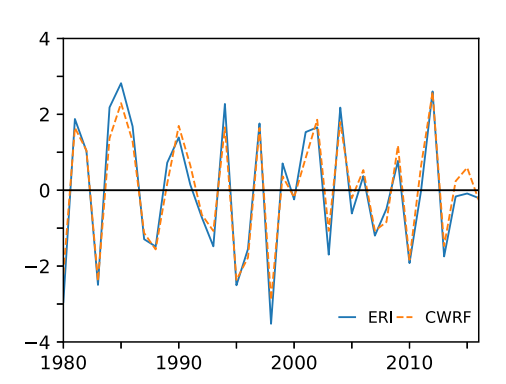


FIGURE 11 East Asian summer monsoon index (EASMI) from 1980 to 2016 (black line denotes the climatological mean; orange curve denotes the simulation; blue curve denotes the reanalysis) [Colour figure can be viewed at wileyonlinelibrary.com]

Sea before then forming a strong airstream flowing northwards along the western ridge of WPSH. The other two channels originate from the Australian high and the western Pacific Ocean. The simulation shows an anomalous anticyclonic circulation departures from the reanalysis over the Sea of Japan (Figure 12c), where the

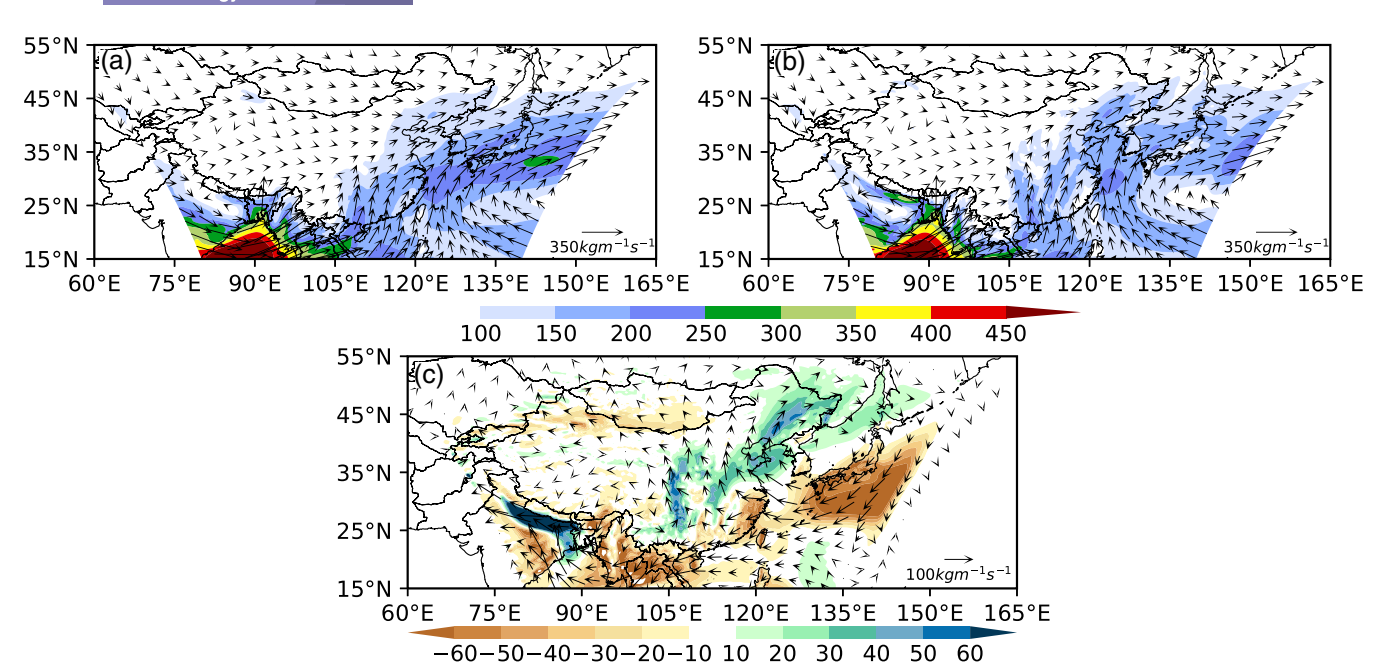


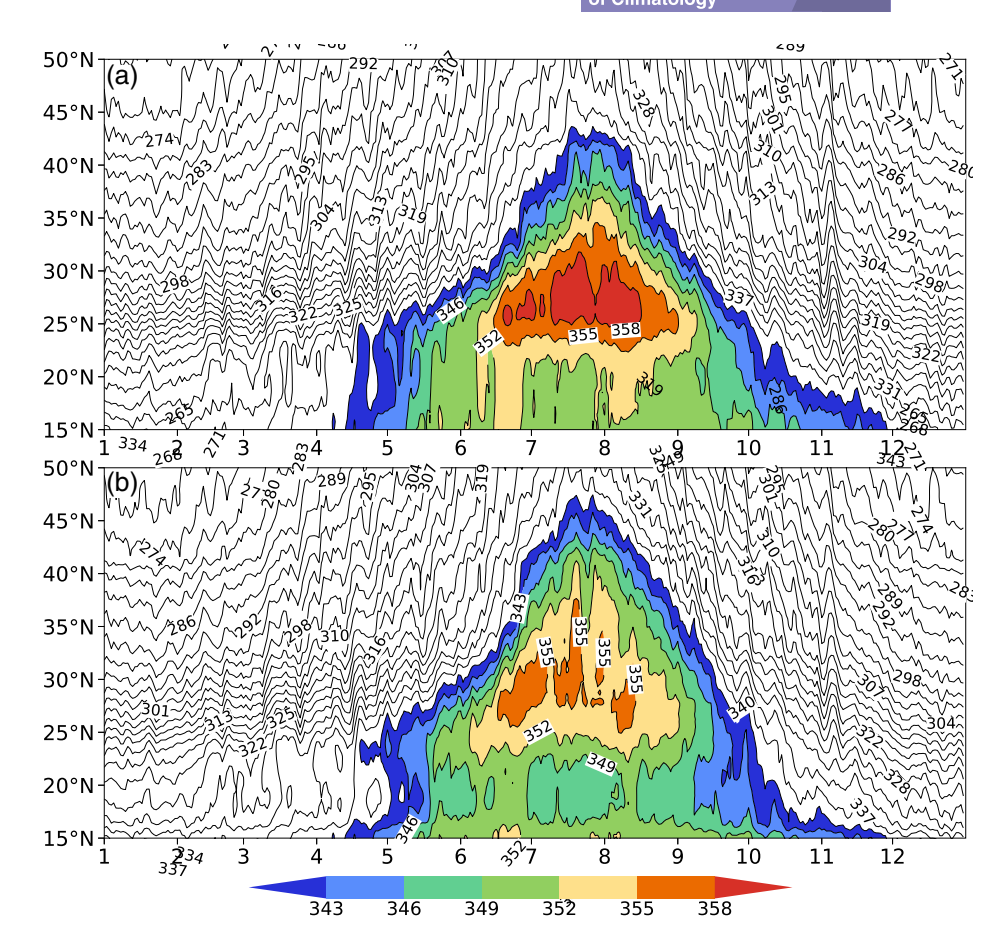
FIGURE 12 Climatological mean 1,000–300 hPa vertically integrated moisture transport flux (units: kg/m/s) in summer (June–July–August): (a) reanalysis; (b) simulation; (c) simulation minus reanalysis [Colour figure can be viewed at wileyonlinelibrary.com]

southerly in the northwest contributes to northward water vapour transport and thus leads to stronger moisture convergence over North China and the Sea of Japan and more rainfall over North China (Figure 3). The northerly in the south weakens water vapour transport to South China and thus leads to weaker moisture flux over South China, the East China Sea and Japan, as well as less rainfall over South China (Figure 3c). The other strong easterly occurs over the South China Sea, Indochina Peninsula, and the northern subcontinent. It weakens the advance of the southwest monsoon to East Asia and thus leads to weaker water vapour transport and less rainfall over Southwest China.

The EASM flows across the tropical ocean with abundant moisture (Li et al., 2005). When it enters the mainland, temperature rises due to radiative heating. Therefore, the air mass is rich in heat and moisture. Pseudo-equivalent temperature (θ_{se}), as a physical variable combining temperature and water vapour, can well reflect frontal zones and unstable conditions. The 340-K isoline at 850 hPa is usually used to represent the thermodynamic property of warm and moist air masses (Ding et al., 2018). As shown in Figure 13a, the lower troposphere in East Asia is obviously drier before than after mid-April. With the pre-flood season of South China starting in mid-April, the warm and moist air masses are gradually pushed northwards from the tropical ocean south of 20°N. In mid-May, with the onset of the South China Sea summer monsoon, the warm and moist air masses gradually advance to regions south of the Yangtze River, which is consistent with the northward advancement of the rain band. In mid-June, the centre of maximum θ_{se} appears around 30°N and lasts for a long period until mid-August, when the northernmost location of the 340-K isoline reaches to around 43°N and then shifts southwards rapidly. In early September, the centre of maximum θ_{se} abruptly disappears. After October, the 340-K isoline completely retreats from the mainland (Figure 13a). The simulations are generally in good agreement with the reanalysis. However, the model simulates the pre-flood season of South China delayed by about 15 days, the location of maximum θ_{se} shifted northwards by 2°, the intensity slightly weaker, and the northern ridge of the 340-K isoline located further north (exceeding 45°N). All these biases may lead to more rainfall over North China and less over the Yangtze River basin (Figure 13b).

The height–latitude cross-section of θ_{se} and specific humidity (Figure 14) shows that the isolines are both arched to the upper level over the Meiyu region, which exceeds 500 hPa. It resembles a tropical cyclone structure with a warm core. The θ_{se} decreases with height, and convection instability is prone to occur. In the middle and high latitudes (north of 40° N), the convective instability layer mainly locates between 900 and 600 hPa and becomes thinner as it is in farther north. The dense isoline area of θ_{se} is around 40° N, where the frontal zone exists. The simulation is close to the reanalysis except that it underestimates the warm core over the Meiyu region, with colder central temperature by over 4 K,

FIGURE 13 Latitude–time cross-section of averaged θ_{se} at 850 hPa along 110°–120°E from January to December (units: K; colour shading denotes $\theta_{se} \ge 340$ K): (a) reanalysis; (b) simulation [Colour figure can be viewed at wileyonlinelibrary.com]



weaker convective intensity and drier specific humidity. The other warm core with an opposite bias occurs at 35°–45°N mainly in the lower troposphere (below 700 hPa), with warmer central temperature by over 4 K, stronger convective intensity and wetter specific humidity. This bias distribution is conducive to rainfall underestimate over South China and overestimate over North China (Figures 3c and Figure 4b).

4 | SUMMARY AND CONCLUSIONS

This study presented a comprehensive analysis of the CWRF simulation of the East Asian summer monsoon characteristics during 1980–2016 and investigated the possible causes for the model biases. The main findings are summarized below:

CWRF reasonably simulates the intensity and position of high temperatures in summer. High interannual TCCs of summer temperatures occur over most parts of China, exceeding 0.6 over Northeast–Northwest China. Positive (negative) temperature biases mainly locate north (south) of 30°N, and low TCCs appear over the Yellow River–Yangtze River basin. The model also exhibits good performance in simulating rainfall over Northeast

China, Southeast (coastal) China, Tibet, and parts of Xinjiang. It reproduces the sub-seasonal precipitation variation and the rain band south–north movement over East China. CWRF overestimates rainfall mainly over North China and underestimates it over South China. These biases are associated with more intense summer monsoon, causing rainfall overestimate over the north and underestimate over the Yangtze–HuaiheRiver basin.

CWRF successfully reproduces the large-scale circulation patterns as in the reanalysis, including the location and intensity of key pressure and wind systems and their variations. In particular, the model well simulates the northward advance and southward retreat of WPSH as associated with the EASM developing and decaying phases, respectively. However, the simulated WPSH centre is slightly weaker and its position is more eastward than the reanalysis. Positive geopotential height biases occur over Mongolia and East China, which leads to higher temperatures and more rainfall over North China. These biases may result from multiple factors. Updating vegetation leaf area index distribution in CWRF can reduce precipitation (negative) and temperature (positive) biases in the Yangtze River basin, and so can adjusting the rain conversion rate in the cumulus parameterization as well as improving the land surfacesubsurface flow coupling and cloud-aerosol-radiation

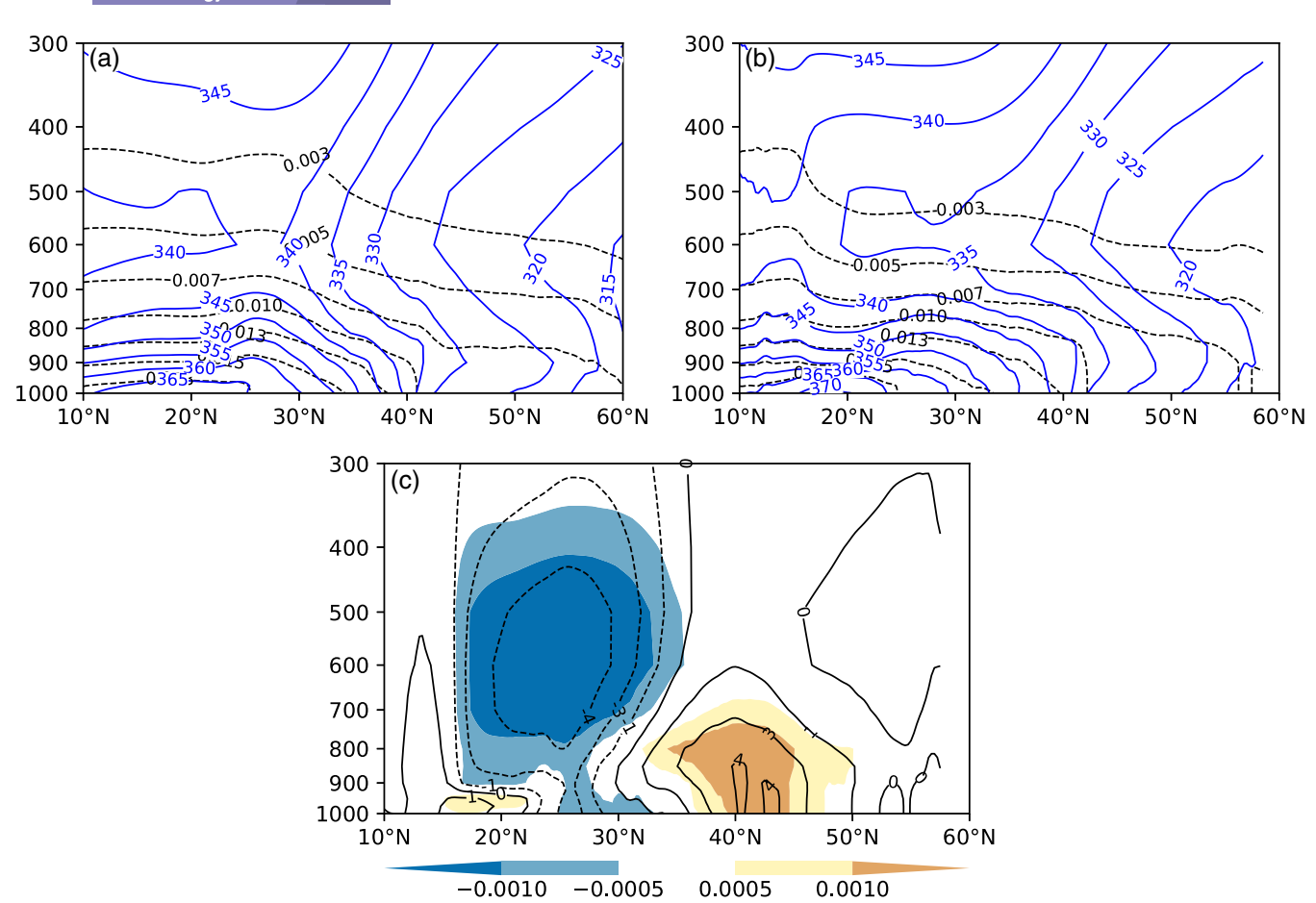


FIGURE 14 Height-latitude cross-section of averaged θ_{se} (units: K) and specific humidity (units: kg/kg) along 110°-120°E in summer (June–July–august) [blue and black curves denote θ_{se} and specific humidity, respectively, in (a) and (b); colour shading in (c) denotes θ_{se} deviation and contours denote specific humidity deviation (dotted and solid curves of which denote negative and positive values, respectively): (a) reanalysis; (b) simulation; (c) simulation minus reanalysis [Colour figure can be viewed at wileyonlinelibrary.com]

interaction (manuscripts in preparation). In addition, CWRF currently does not consider human interventions, such as agricultural production and irrigation, which may have significant impacts on surface temperature and precipitation (e.g., Yang *et al.*, 2016).

The simulated geopotential height at 500 hPa is generally consistent with the reanalysis. Positive biases appear over northeastern East Asia and negative biases over the Qinghai-Tibet Plateau (Figure 5), which results in systematic overestimate of the land-ocean thermal contrast. These biases cause thermodynamic responses in EASM that strengthen China summer monsoon and advance it more northwards, and consequently shift the rain band more northwards. Note, however, that largescale circulations and regional precipitation are fully coupled, where the former provides energy and water supplies for convection to occur and the latter produces feedback to the system through condensational heat release (Lu and Lin, 2009; Yang et al., 2015). It is critical to conduct more comprehensive diagnosis of sensitivities to model physics/dynamics configurations to disentangle the complex processes underlying these model biases (Sun and Liang, 2020b).

CWRF well simulates the EASM index variations during 1980-2016, producing a correlation coefficient with the reanalysis as high as .97. The model exhibits good performance in simulating the summer mean circulations, including the upper and lower level jets, South Asian high and water vapour transport. However, regional biases still exist. In particular, weak biases of an anticyclonic (cyclonic) circulation at 200 hPa occur over Southeast China (Tibetan Plateau), and correspondingly WSPH is shifted northwards and the South Asian high northeastwards. Meanwhile, biases of an anticyclonic circulation occur at 850 hPa over the southern Sea of Japan, accompanied with the summer monsoon expanded northwards and more rainfall over North China. In addition, the simulated water vapour fluxes are more intense in middle and high latitudes but weaker in lower latitudes, which also favours the rain band shifted more northwards and thus causes rainfall overestimate over North China and underestimate over South China.

ATEX and arctic air-mass data sets. Quarterly Journal of the Royal Meteorological Society., 112(473), 693–709.

In conclusion, CWRF well captures the summer mean circulation and regional climate over East Asia, as well as the seasonal evolution of the monsoon circulation systems and the seasonal south-north movement of rain bands over East China. However, notable biases still exist, requiring further model improvements. Summer mean geopotential height shows positive biases over Northeast Asia and negative biases over the ocean, and so the land-ocean thermal contrast is overestimated in the model. As a result, the simulated WPSH is more intense and shifted more northwards, accompanied with a stronger EASM and regional biases in surface temperature and rainfall over China. CWRF has incorporated tremendously more alternate physics schemes than the control configuration presented here (Liang et al., 2012, 2018; Liang and Zhang, 2013; Sun and Liang, 2020a). The control version used in this study does not represent the best performance of CWRF, since it is only a single configuration combining one specific scheme among many alternates each of the seven major physics processes. There is large room to improve the CWRF performance particularly on EASM by optimizing the physics configuration or likely multi-physics ensemble through systematic sensitivity studies and comprehensive process understanding (Sun and Liang, 2020b). Nevertheless, our bias analysis and diagnostic understanding presented above offer important guidelines for future

ACKNOWLEDGEMENTS

This study was jointly supported by the Second Tibetan Plateau Scientific Expedition and Research Program of China (Grant No. 2019QZKK0208), the Strategic Priority Research Program of the Chinese Academy of Sciences (Grant No. XDA20100304), the National Natural Science Foundation of China (Grant No.41790471), and the National Key Scientific Research Plan of China (Grant Nos. 2016YFA0602200). Liang was partially supported by U.S. National Science Foundation Innovations at the Nexus of Food, Energy and Water Systems under Grant EAR1903249.

model refinements targeting at EASM prediction.

ORCID

Qingquan Li https://orcid.org/0000-0002-4133-6518 Chongbo Zhao https://orcid.org/0000-0002-1828-4713

REFERENCES

- Betts, A.K. (1986) A new convective adjustment scheme. Part I: observational and theoretical basis. *Quarterly Journal of the Royal Meteorological Society*, 12(473), 677–691.
- Betts, A.K. and Miller, M.J. (1986) A new convective adjustment scheme. II: single column tests using GATE wave, BOMEX,

- Bretherton, C.S. and Park, S. (2009) A new moist turbulence parameterization in the community atmosphere model. *Journal of Climate*, 22, 3422–3448.
- Choi, H.I., Kumar, P. and Liang, X.-Z. (2007) Three-dimensional volume-averaged soil moisture transport model with a scalable parameterization of sub-grid topographic variability. Water Resource Research, 43, W04414.
- Choi, H.and Liang, X-Z. (2010) Improved terrestrial hydrologic representation in mesoscale land surface models. *Journal of Hydrometeorology*, 11797–809.
- Choi, H.I., Liang, X.-Z. and Kumar, P. (2013) A conjunctive surface subsurface flow representation for mesoscale land surface models. *Journal of Hydrometeorology*, 14, 1421–1442.
- Chou, M-D, Suarez, MJ. (1999). A solar radiation parameterization for atmospheric studies. (Last revision on March 2002) technical report series on global modeling and data assimilation. In: Suarez, M. J. (Ed.), *NASA/TM-1999-104606*, Vol. 15. Greenbelt, MD: Goddard Space Flight Center, 42 pp.
- Chou, M-D, Suarez, MJ, Liang, X-Z, Yan Michael, M.-H. (2001). A thermal infrared radiation parameterization for atmospheric studies. (Last revision on July 2002) technical report series on global modeling and data assimilation. In: Suarez, M. J. (Ed.), NASA/TM-2001-104606, Vol. 19, pp. 56. Greenbelt, MD: Goddard Space Flight Center.
- Dee, D.P., Uppala, S.M., Berrisford, P., Poli, P., Kobayashi, S., Andrae, U., Balmaseda, M.A., Balsamo, G., Bauer, P., Bechtold, P., Beljaars, A.C.M., Van de berg, L., Bidlot, J., Bormann, N., Delsol, C., Dragani, R., Fuentes, M., Geer, A.J., Haimberger, L., Healy, S.B., Hersbach, H., Hólm, E.V., Isaksen, L., Kållberg, P., Köhler, M., Matricardi, M., McNally, A.P., Monge-Sanz, B.M., Morcrette, J.-J., Park, B.-K., Peubey, C., De Rosnay, P., Tavolato, C., and Thépaut, J.-N. (2011) The ERA-interim reanalysis: configuration and performance of the data assimilation system. *Quarterly Journal of the Royal Meteorological Society*, 137, 553–597.
- Dickinson, R.E., Errico, R.M., Giorgi, F. and Bates, G.T. (1989) A regional climate model for the western United States. *Climatic Change*, 15(3), 383–422.
- Ding, Y., Liu, Y., Shi, X., Li, Q., Li, Q. and Liu, Y. (2006b) Multiyear simulations and experimental seasonal predictions for rainy seasons in China by using a nested regional climate model (RegCM_NCC) part II: the experimental seasonal prediction. *Advances in Atmospheric Sciences*, 23(4), 487–503.
- Ding, Y., Shi, X., Liu, Y., Liu, Y., Li, Q., Qian, Y., Miao, M., Zhai, G. and Gao, K. (2006a) Multi-year simulations and experimental seasonal predictions for rainy seasons in China by using a nested regional climate model (RegCM_NCC) part I: sensitivity study. *Advances in Atmospheric Sciences*, 23(3), 323–341.
- Ding, Y., Si, D., Liu, Y. and Wang, Z. (2018) On the characteristics, driving forces and inter-decadal variability of the East Asian summer monsoon. *Chinese Journal of Atmospheric Sciences* (in Chinese), 42(3), 533–558.
- Emanuel, K.A. (1991) A scheme for representing cumulus convection in large-scale models. *Journal of the Atmospheric Sciences*, 48(21), 2313–2329.
- Gao, X., Shi, Y., Zhang, D. and Giorgi, F. (2012) Climate change in China in the 21st century as simulated by a high resolution regional climate model. *Chinese Science Bulletin*, 57, 1188–1195.

- Giorgi, F. (2006) Regional climate modeling: status and perspectives. *Journal de Physique IV*, 139, 101–118.
- Giorgi, F. and Bates, G.T. (1989) The climatological skill of a regional model over complex terrain. *Monthly Weather Review*, 117(11), 2 325–2 347.
- Giorgi, F., Coppola, E., Solmon, F. and Mariotti, L. (2011) RegCM4: model description and preliminary tests over multiple COR-DEX domains. *Climate Research*, 936(1), 577X.
- Giorgi, F. and Gutowski, W.J. (2015) Regional dynamical downscaling and the CORDEX initiative. *Annual Review of Environment and Resources*, 40, 467–490.
- Holtslag, A.M. and Boville, B.A. (1993) Local versus nonlocal boundary layer diffusion in a global climate model. *Journal of Climate*, 6, 1825–1842.
- Hu, Z.-Z., Kumar, A., Jha, B. and Huang, B. (2019) How much of monthly mean precipitation variability over global land is associated with SST anomalies? *Climate Dynamics*, 54, 701–712. https://doi.org/10.1007/s00382-019-05023-5.
- Kahn, R.A., Gaitley, B.J., Martonchik, J.V., Diner, D.J., Crean, K.A. and Holben, B. (2005) Multiangle imaging spectroradiometer (MISR) global aerosol optical depth validation based on 2years of coincident Aerosol Robotic Network (AERONET) observations. *Journal of Geophysical Research*, 110, D10S04.
- Kahn, R.A., Garay, M.J., Nelson, D.L., Yau, K.K., Bull, M.A., Gaitley, B.J., Martonchik, J.V. and Levy, R.C. (2007) Satellitederived aerosol optical depth over dark water from MISR and MODIS: comparisons with AERONET and implications for climatological studies. *Journal of Geophysical Research*, 112, D18205.
- Li, Q., Wang, J., Yang, S., Wang, F., Wu, J. and Hu, Y. (2020) Subseasonal prediction of rainfall over the South China Sea and its surrounding areas during spring-summer transitional season. *International Journal of Climate*, 40, 1–21. https://doi.org/10.1002/joc.6456.
- Li, Q., Yang, S., Kousky, V.E., Higgins, R.W., Lau, K.M. and Xie, P. (2005) Features of cross-Pacific climate shown in the variability of China and US precipitation. *International Journal of Clima*tology, 25, 1675–1696.
- Liang, P., Hu, Z.-Z., Liu, Y., Yuan, X., Li, X. and Jiang, X. (2019) Challenges in predicting and simulating summer rainfall in the eastern China. *Climate Dynamics*, 52(3–4), 2217–2233.
- Liang, X.-Z., Choi, H., Kunkel, K.E., Dai, Y., Joseph, E., Wang, J. and Kumar, P. (2005a) Surface boundary conditions for mesoscale regional climate models. *Earth Interactions*, 9, 1–28.
- Liang, X.-Z., Kunkel, K.E. and Samel, A.N. (2001) Development of a regional climate model for U. S. Midwest applications. Part I: sensitivity to buffer zone treatment. *Journal of Climate*, 14(23), 4363–4378.
- Liang, X.-Z., Sun, C., Zheng, X., Dai, Y., Xu, M., Choi, H., Ling, T., Qiao, F., Kong, X., Bi, L. and Wang, F. (2018) CWRF performance at downscaling China climate characteristics. *Climate Dynamics*, 52, 2159–2184.
- Liang, X.-Z. and Wang, W.-C. (1998) Associations between China monsoon rainfall and tropospheric jets. Quarterly Journal of the Royal Meteorological Society, 124, 2597–2623.
- Liang, X.-Z., Xu, M., Choi, H.I., Kunkei, K.E., Rontu, L., Wang, J. (2006b). Development of the regional Climate Weather Research and Forecasting Model (CWRF): Treatment of

- subgrid topography effects. In: Proceedings of the 7th Annual WRF User's Workshop, Boulder, CO, June 19-22, 5 pp.
- Liang, X.-Z., Xu, M., Gao, W., Kunel, K., Slusser, J., Dai, Y., Min, Q., Houser, P.R., Rodell, M., Schaaf, B.S. & Gao, F., et al. (2005b) Development of land surface albedo parameterization based on moderate resolution imaging Spectroradiometer (MODIS) data. *Journal of Geophysical Research*, 110, D11107. https://doi.org/10.1029/2004JD005579.
- Liang, X.-Z., Xu, M., Yuan, X., Ling, T., Choi, H.I., Zhang, F., Chen, L., Liu, S., Su, S., Qiao, F., He, Y., Wang, J.X.L., Kunkel, K.E., Gao, W., Joseph, E., Morris, V., Yu, T.W., Dudhia, J. and Michalakes, J. (2012) Regional climate-weather research and forecasting model (CWRF). Bulletin of the American Meteorological Society, 93, 1363–1387.
- Liang, X.-Z., Xu, M., Zhu, J., Kunkei, K.E., Rontu, L., Wang, J. (2005c). Development of the regional climate-weather research and forecasting model (CWRF): Treatment of topography. In: Proceedings of the 2005 WRF/MMS User's Workshop, Boulder, CO, June 27–30, 5pp.
- Liang, X.-Z. and Zhang, F. (2013) The cloud-aerosol-radiation (CAR) ensemble modeling system. Atmospheric Chemistry and Physics, 13, 8335–8364.
- Ling, T.-J., Liang, X.-Z., Xu, M., Wang, J. and Noh, Y. (2011) A multilevel ocean mixed-layer model for 2-dimension applications. Acta Oceanol Sinica (In Chinese), 33(03), 1–10.
- Ling, T.-J., Xu, M., Liang, X.-Z., Wang, J.L.X.L. and Noh, Y. (2015) A multi-level ocean mixed layer model resolving the diurnal cycle: development and validation. *Journal of Advances in Modeling Earth Systems*, 7, 1680–1692.
- Liu, S., Liang, X.-Z., Gao, W. and Zhang, H. (2008) Application of climate-weather research and forecasting model (CWRF) in China: domain optimization. *Chinese Journal of Atmospheric* Sciences (in Chinese), 32(3), 457–468.
- Lu, R. and Lin, Z. (2009) Role of subtropical precipitation anomalies in maintaining the summertime meridional teleconnection over the Western North Pacific and East Asia. *Journal of Climate*, 22, 2058–2072.
- Ou, T., Chen, D., Linderholm, H.W. and Jeong, J.H. (2013) Evaluation of global climate models in simulating extreme precipitation in China. *Tellus A*, 65(5), 19799. https://doi.org/10.3402/tellusa.v65i0.19799.
- Qiao, F. & Liang, X-Z. (2015) Effects of cumulus parameterizations on predictions of summer flood in the Central United States. Climate Dynamics, 45727–744.
- Qiao, F. and Liang, X-Z. (2016b) Effects of cumulus parameterization closures on simulations of summer precipitation over the continental United States. *Climate Dynamics*, 49225–247.
- Qiao, F. and Liang, X-Z. (2016a) Effects of cumulus parameterization closures on summer precipitation simulation over the United States coastal oceans.. *Journal of Advances in Modeling Earth Systems*, 8764–785.
- Qiao, F. and Liang, X.-Z. (2017) Effects of cumulus parameterization closures on simulations of summer precipitation over the continental United States. *Climate Dynamics*, 49, 225–247.
- Rontu, L. (2006) A study on parameterization of orography-related momentum fluxes in a synoptic-scale NWP model. *Tellus*, 58, 69–81.

- Si, D., Zhao, P. and Wang, M. (2019) Inter-decadal change of the middle-upper tropospheric land-sea thermal contrast in the late 1990s and the associated northern hemisphere hydroclimate. *International Journal of Climatology*, 39(7), 3271–3281.
- Skamarock, W.C., Klemp, J.B., Dudhia, J, Gill, D.O., Barker, D., Wang, W., Powers, J.G. (2005). A description of the advanced research WRF version 2. NCAR Tech.Note NCAR/TN-486+STR.
- Sun, C. and Liang, X.-Z. (2020a) Improving U.S. extreme precipitation simulation: sensitivity to physics parameterizations. *Climate Dynamics*, 54, 4891–4918.
- Sun, C. and Liang, X.-Z. (2020b) Improving U.S. extreme precipitation simulation: dependence on cumulus parameterization and underlying mechanism. *Climate Dynamics*, 55, 1325–1352. https://doi.org/10.1007/s00382-020-05328-w.
- Tao, W.-K., Simpson, J., Baker, D., Braun, S., Chou, M.D., Ferrier, B., Johnson, D., Khain, A., Lang, S., Lynn, B., Shie, C. L., Starr, D., Sui, C.H., Wang, Y. and Wetzel, P. (2003) Microphysics, radiation and surface processes in the Goddard cumulus ensemble (GCE) model. *Meteorology and Atmospheric Physics*, 82, 97–137.
- Tapiador, F.J., Navarro, A., Moreno, R., Sánchez, J.L. and García-Ortega, E. (2020) Regional climate models: 30 years of dynamical downscaling. *Atmospheric Research*, 235(2020), 104785.
- WMO. 2006. Standardised Verification System (SVS) for Long-Range Forecasts (LRF): New attachment II-8 to the manual on the GDPFS (WMO-No. 485), Volume I.
- Wu, J. and Gao, X. (2013) Gridded daily observation dataset over China region and comparison with the other datasets. *Chinese Journal of Geophysics*, 56(4), 1102–1111.
- Xu, K.-M. and Randall, D.A. (1996) A semiempirical cloudiness parameterization for use in climate models. *Journal of the Atmospheric Sciences*, 53, 3084–3102.
- Xu, M. and Liang, X-Z. (2014) MODIS consistent vegetation parameter specifications and their impacts on regional climate simulations. *Climate Dynamics*, 278578–8596.
- Xu, Z., Han, Y. and Yang, Z. (2019) Dynamical downscaling of regional climate: a review of methods and limitations. *Science China(Earth Sciences)*, 62(2), 365–375.
- Xue, Y., Janjic, Z., Dudhia, J., Vasic, R. and Sales, F. D. (2014) A review on regional dynamical downscaling in intraseasonal to seasonal simulation/prediction and major factors that affect downscaling ability. *Atmospheric Research*, 147–148, 68–85.
- Yang, B., Zhang, Y., Qian, Y., Huang, A. and Yan, H. (2015) Calibration of a convective parameterization scheme in the WRF model and its impact on the simulation of east Asian summer monsoon precipitation. *Climate Dynamics*, 44(5–6), 1661–1684.

- Yang, B., Zhang, Y., Qian, Y., Tang, J. and Liu, D. (2016) Climatic effects of irrigation over the Huang-Huai-Hai plain in China simulated by the weather research and forecasting model. Journal of Geophysical Research – Atmospheres, 121, 2246–2264.
- Yuan, X. and Liang, X-Z. (2011) Evaluation of a Conjunctive Surface-Subsurface Process model (CCSP) over the contiguous United States at regional-local scales. *Journal of Hydrometeorology*, 12579–599.
- Zeng, M., Lu, W., Liang, X.-Z. and Wang, X. (2008) Ensemble forecast experiment on precipitation in summer by CWRF numerical model. *Plateau Meteorology (In Chinese)*, 27(6), 1 218–1 1228.
- Zeng, M., Lu, W., Liang, X.-Z., Wang, W. and Zhou, J. (2009) Numerical simulation of influence of the topography on continuous freezing disaster distribution occurred south of China at the beginning of 2008. *Plateau Meteorology (In Chinese)*, 28(6), 1376–1387.
- Zhang, Q., Tao, S. and Chen, L. (2003) The inter-annual variability of east Asian summer monsoon indices and its association with the pattern of general circulation over East Asia. *Acta Meteorologica Sinica (In Chinese)*, 61(4), 559–568.
- Zhang, F., Liang, X-Z. and Zeng, Q. (2013) Dominant roles of subgridscale cloud structures in model diversity of cloud radiative effects. *Journal of Geophysical Research*, 1187733–7749.
- Zhang, T., Yang, S., Jiang, X. and Dong, S. (2016) Sub-seasonal prediction of the maritime continent rainfall of wet-dry transitional seasons in the NCEP climate forecast version 2. *Atmosphere*, 7(2), 28–39.
- Zhang, T., Yang, S., Jiang, X. and Zhao, P. (2015) Seasonal-interannual variation and prediction of wet and dry season rainfall over the maritime continent: roles of ENSO and monsoon circulation. *Journal of Climate*, 29(10), 3675–3695.
- Zhao, G., Girolamo, L.D., Dey, S., Jones, A.L. and Bull, M. (2009) Examination of direct cumulus contamination on MISRretrieved aerosol optical depth and angstrom coefficient over ocean. *Geophysical Research Letters*, 36, L13811.

How to cite this article: Li Q, Wang T, Wang F, *et al.* Dynamical downscaling simulation of the East Asian summer monsoon in a regional Climate-Weather Research and Forecasting model. *Int J Climatol.* 2020;1–17. https://doi.org/10.1002/joc.6800